Ultrasonics 169 (2027) 108278

Contents lists available at ScienceDirect

Ultrasonics

journal homepage: www.elsevier.com/locate/ultras

Reduced-parameter ultrasound electrical impedance spectroscopy for characterization of piezoelectric transducers and polymer materials

Jhoan F. Acevedo-Espinosa [a,b], Flávio O.S. D'Amato [b], Marcos V.D. Vermelho [c], Alana K.X.B. Branco [d], Antônio A.O. Carneiro [e], Michäel Baudoin [f], Joao L. Ealo [g], Glauber T. Silva [b,*]

[a] School of Civil and Geomatics Engineering and Center for Bioinformatics and Photonics-CIBioFi, Universidad del Valle, Cali, Colombia
[b] Group of Acoustical Physics & Microfluidics, Institute of Physics, Federal University of Alagoas, Maceió, Alagoas, Brazil
[c] Laboratory of Applied Microtechnology, Federal University of Alagoas, Maceió, Alagoas, Brazil
[d] Campus of Engineering and Agricultural Sciences, Federal University of Alagoas, Rio Largo, Alagoas, Brazil
[e] Department of Physics, FFCLRP, University of São Paulo, Ribeirão Preto, São Paulo, Brazil
[f] Université de Lille, IEMN, Université Polytechnique Hauts-de-France, Lille, France
[g] School of Mechanical Engineering and Center for Bioinformatics and Photonics-CIBioFi, Universidad del Valle, Cali, Colombia

ARTICLE INFO

Keywords:
Material characterization using ultrasound
Ultrasound devices
Transducers
And systems
Physical ultrasound
Ultrasonic wave propagation
Acoustofluidics

ABSTRACT

This work presents a reduced-parameter ultrasound electrical impedance spectroscopy (RP-UEIS) framework for estimating the complex electromechanical parameters of piezoelectric transducers — specifically lead zirconate titanate (PZT) ceramics — and the viscoelastic properties of polymer materials. The method combines a low-cost electrical impedance spectroscopy setup with an inverse finite-element fitting procedure to identify material parameters from measured impedance spectra. A sensitivity-based parameter analysis of the transducer reduces the dimensionality of the inverse problem from sixteen to ten parameters, significantly improving computational efficiency. Once the transducer parameters are calibrated, the viscoelastic properties of polymer samples can be identified in approximately one hour, compared with the ∼10 hours typically required by the original UEIS method. Using a PZT-4 reference transducer, complex elastic moduli and acoustic attenuation parameters are estimated at 1 MHz for several polymeric materials commonly used in additive and subtractive manufacturing. The RP-UEIS framework is further demonstrated through the design of an acoustofluidic chip, where the identified polylactic acid (PLA) parameters are incorporated into a finite-element model of a circular half-wavelength resonator. RP-UEIS provides a practical and efficient tool for the characterization of polymer materials and for physically consistent parameter estimation in the modeling of polymer-based acoustofluidic devices.

1. Introduction

Polymer material characterization under mechanical excitation in the megahertz frequency range remains an active and challenging research topic. This difficulty is relevant to several ultrasonic technologies in which polymers are used as structural elements, bonding layers, or microfabricated substrates, including biomedical ultrasound [1] and acoustic sensors [2]. In acoustofluidics, which combines ultrasonic wave in microfluidic units, polymer materials have been used to validate acoustophoresis models in 3D-printed platforms [3], polymer-based devices [4], and chips to enable cell spheroids formation [5]. A subsequent 3D-printed acoustofluidic platform further demonstrated the integration of polymeric device fabrication with Raman-based cell analysis [6,7]. More recently, 3D printed acoustofluidic systems have also been used for cell microculture applications [8]. The dynamic mechanical response of these materials at ultrasonic frequencies is governed by complex viscoelastic behavior, where both elastic stiffness and energy dissipation mechanisms play an important role.

In addition, the mechanical properties of polymer materials can vary significantly due to uncontrolled chemical reactions during fabrication, curing conditions, and post-processing procedures. As a consequence, the complex elastic moduli reported for polymers at megahertz frequencies are often strongly dependent on the specific fabrication route of the material samples, which significantly limits the usefulness of such data for predictive numerical modeling of ultrasonic devices.

As manufacturing methods such as 3D printing, laser CNC machining, and soft lithography become increasingly popular in ultrasonic

* Corresponding author.
E-mail address: gtomaz@fis.ufal.br (G.T. Silva).

https://doi.org/10.1016/j.ultras.2026.108278
Received 17 March 2026; Received in revised form 4 August 2026; Accepted 17 August 2026
Available online 3 September 2026

device fabrication, the diversity of polymer fabrication routes continues to grow. Consequently, there is an increasing need for straightforward and reliable methods to characterize the material properties of polymers used in these devices.

A variety of experimental techniques have been developed to determine the mechanical properties of polymer materials. Several experimental methods have been developed to determine the elastic and dissipative properties of solid materials. Resonant ultrasound spectroscopy has been used to extract elastic tensors from solid specimens [9], whereas impulse excitation methods have been applied to identify elastic moduli and material damping [10]. Ultrasonic characterization methods are also particularly relevant in this context because they probe material response in frequency ranges closer to those considered in the present work. Pulse-echo measurements have been used to determine acoustic properties of polymers [11], ultrasonic testing has been applied to investigate wave propagation in polymeric materials [12], and related approaches have recently been extended to 3D-printed polymer structures [13]. However, these techniques typically characterize bulk samples and therefore do not capture the coupled dynamics that arise in multilayer systems composed of piezoelectric transducers, bonding layers, and structural polymers.

The characterization of materials within assembled ultrasonic devices has motivated indirect methods based on the electromechanical response of the complete system. Electrical impedance measurements of piezoelectric resonators have been used to extract piezoelectric coefficients from resonance and antiresonance behavior [14], with later formulations incorporating complex material coefficients to account for losses [15]. Related inverse approaches fitted selected impedance resonances to analytical or numerical transducer models [16]. In parallel, reduced-order equivalent-circuit models became widely used: the Mason model couples the electrical and mechanical domains through a network representation [17], whereas the KLM model provides a computationally efficient transmission-line description of piezoelectric wave propagation [18].

Although computationally efficient, one-dimensional equivalent-circuit models cannot fully describe complex geometries, multidimensional wave fields, or heterogeneous loading. This limitation has motivated impedance-based methods that use the electrical response of a bonded or loaded piezoelectric element as an indirect probe of the surrounding system. In electromechanical impedance methods (EMIs), variations in the coupled electrical impedance are commonly used to assess structural health, boundary conditions, or mechanical loading [19]. Ultrasound electrical-impedance spectroscopy (UEIS) extends this principle toward quantitative material characterization by combining impedance measurements with three-dimensional numerical optimization to extract complex viscoelastic moduli of soft polymer samples over the kilohertz-to-megahertz range [20]. Despite its advantages, the inverse identification procedure associated with UEIS typically involves a high-dimensional parameter space, which can lead to computationally demanding optimization problems.

In this work, we introduce a reduced-parameter ultrasound electrical impedance spectroscopy (RP-UEIS) framework. The proposed approach combines impedance measurements with inverse finite-element modeling and sensitivity analysis to identify the most influential system parameters. This parameter estimation from impedance spectra is formulated as an inverse problem, a framework widely used in the modeling of piezoelectric devices and multiphysics systems [21], as well as in general parameter estimation theory [22]. Specifically, our strategy reduces the dimensionality of the inverse problem from 16 parameters in the original UEIS formulation to 10 parameters, significantly improving computational efficiency without sacrificing predictive accuracy. Moreover, the parameters obtained with RP-UEIS should be interpreted as effective values valid over a narrow frequency band around the resonance frequency of the PZT disc. This local characterization is well suited for ultrasonic devices that operate within a limited spectral bandwidth.

Using a PZT-4 disc, the RP-UEIS framework is applied to characterize several polymer materials commonly used in additive and subtractive manufacturing, namely polylactic acid (PLA), acrylonitrile butadiene styrene (ABS), glycol-modified polyethylene terephthalate (PET-G), polymethyl methacrylate (PMMA), and epoxy resin. The resulting complex elastic moduli and acoustic attenuation parameters are estimated near 1 MHz. Although the RP-UEIS framework can in principle be extended to other ultrasonic frequency ranges, this study focuses on 1 MHz because the first thickness-mode resonance provides a well-isolated impedance peak, improving numerical stability. Higher-order modes or higher frequencies, such as 10 MHz, increase modal coupling and require thinner piezoceramics, thereby tightening fabrication tolerances. The 1 MHz range is also a practical benchmark for low-cost polymer acoustofluidics, balancing wavelength, attenuation, and transducer availability. Consequently, the identified parameters should be interpreted as effective values for this narrow operating band. Finally, the estimated parameters of PLA and epoxy materials are incorporated into a finite-element model of an acoustofluidic chip (acoustochip) consisting of a circular half-wavelength resonator. This example demonstrates how the proposed methodology provides physically consistent material parameters suitable for finite-element modeling and design of polymer-based acoustofluidic devices near their operating resonance.

2. Physical model

The physical modeling framework considers three configurations. The first corresponds to an isolated PZT disc depicted in Fig. 1(a), where the top and lateral boundaries remain free, while the second consists of the PZT coupled to a test material via a thin coupling gel layer (Fig. 1(b)); both are employed in the RP-UEIS method. The third configuration replaces the test material with a acoustochip (Fig. 1(c)) composed of a liquid-filled circular cavity and layers formed by PLA, epoxy, and glass.

The subsequent subsections provide a rigorous formulation of the governing equations, constitutive models, coupling interfaces, and boundary conditions implemented in the numerical framework.

2.1. Time-harmonic excitation

The excitation applied to the PZT disc is assumed to be a time-harmonic signal with linear frequency f and angular frequency $\omega = 2\pi f$. Under this assumption, any physical field can be written as

$$g(\boldsymbol{r}, t) = g(\boldsymbol{r})\, \mathrm{e}^{-\mathrm{i}\omega t}, \tag{1}$$

which reduces the problem to determining the complex-valued spatial amplitude $g(\boldsymbol{r})$. The position vector is expressed in Cartesian coordinates as $\boldsymbol{r} = x_i\, \boldsymbol{e}_i$ ($i = 1, 2, 3$), where x_i are the coordinate components and $\boldsymbol{e}_i$ are the associated orthonormal basis vectors. Hereafter, the Einstein summation convention is adopted for repeated indices.

2.2. Solid materials

The solid layers of the acoustochip are modeled through the linear stress–strain constitutive relation

$$\sigma_{ij} = C_{ijkl}\, \epsilon_{kl}, \tag{2}$$

where C_{ijkl} is the stiffness tensor of the material. The strain components are expressed in terms of the displacement vector field $\boldsymbol{u}(\boldsymbol{r})$ as

$$\epsilon_{ij} = \frac{1}{2}\left(\partial_j u_i + \partial_i u_j\right). \tag{3}$$

The shorthand notation $\partial_i = \partial/\partial x_i$ is adopted here. In the frequency domain, the displacement vector is governed by the linear Cauchy momentum equation involving the stress tensor,

$$-\rho_s \omega^2 \boldsymbol{u} = \boldsymbol{\nabla} \cdot \boldsymbol{\sigma}, \tag{4}$$

where ρ_s denotes the density of the solid medium.

In Voigt notation, the symmetric strain and stress tensors are written as 6×1 matrices,

$$\boldsymbol{\epsilon}_V = \left[\epsilon_{11}\ \epsilon_{22}\ \epsilon_{33}\ 2\epsilon_{23}\ 2\epsilon_{13}\ 2\epsilon_{12}\right]^T, \tag{5a}$$

$$\boldsymbol{\sigma}_V = \left[\sigma_{11}\ \sigma_{22}\ \sigma_{33}\ \sigma_{23}\ \sigma_{13}\ \sigma_{12}\right]^T, \tag{5b}$$

with superscript ^{T} denoting the transpose of a matrix.

We now distinguish between the constitutive descriptions of the PZT disc and the viscoelastic layers. The PZT disc is modeled as a transversely isotropic solid, reflecting its crystallographic symmetry after poling, whereas the polymeric and epoxy layers are treated as fully isotropic materials. In the stiffness-matrix formalism, isotropy is recovered as a special case of transverse isotropy by enforcing specific relations among the elastic coefficients. Accordingly, the stiffness matrix given in Voigt notation is expressed as

$$\mathbf{C}_V = \begin{bmatrix} C_{11} & C_{12} & C_{13} & 0 & 0 & 0 \\ C_{12} & C_{11} & C_{13} & 0 & 0 & 0 \\ C_{13} & C_{13} & C_{33} & 0 & 0 & 0 \\ 0 & 0 & 0 & C_{44} & 0 & 0 \\ 0 & 0 & 0 & 0 & C_{44} & 0 \\ 0 & 0 & 0 & 0 & 0 & C_{66} \end{bmatrix}, \tag{6}$$

with $C_{66} = \left(C_{11} - C_{12}\right)/2$. The stiffness coefficients are complex-valued, $C_{ij} = C'_{ij} + \mathrm{i}\,C''_{ij}$, reflecting storage and loss contributions. We thus have

$$\boldsymbol{\sigma}_V = \boldsymbol{C}_V\,\boldsymbol{\epsilon}_V. \tag{7}$$

2.3. Lead zirconate titanate (PZT) ceramics

A PZT ceramic can be modeled as a transversely isotropic piezoelectric solid, which is compatible with an axisymmetric formulation when both the polarization direction and the applied excitation are aligned with the symmetry axis. It is assumed that the piezoelectric material operates in the quasistatic electric-field approximation, under which electromagnetic wave propagation is negligible. In this regime, the electric field is fully described by the scalar potential ϕ, $\boldsymbol{E} = -\nabla\phi$ and the electric displacement vector is given by the constitutive relation $\boldsymbol{D} = \boldsymbol{\varepsilon}\,\boldsymbol{E}$, with $\boldsymbol{\varepsilon} = \mathrm{diag}\,(\varepsilon_{11}, \varepsilon_{11}, \varepsilon_{33})$ being the permittivity tensor of the transversely isotropic material. We further assume that the material contains no free electric charges. Consequently, Gauss's law reduces to

$$\nabla \cdot \boldsymbol{D} = 0. \tag{8}$$

The linear constitutive relations of piezoelectricity can be written in fully coupled form [23]

$$\sigma_{ij} = C^E_{ijkl}\epsilon_{kl} - e_{kij}E_k, \quad D_i = e_{ijk}\epsilon_{jk} + \varepsilon^{\epsilon}_{ij}E_j, \tag{9}$$

where the superscripts ^{E} and $^\epsilon$ indicate that the elastic stiffness C^E_{ijkl} is evaluated at constant electric field, and the permittivity $\varepsilon^{\epsilon}_{ij}$ is computed at constant strain, respectively. The piezoelectric coupling tensor is defined thermodynamically as $e_{ijk} = \left(\partial D_i/\partial\epsilon_{jk}\right)_E = -\left(\partial\sigma_{jk}/\partial E_i\right)_\epsilon$. Because the strain tensor is symmetric, $\epsilon_{ij} = \epsilon_{ji}$, only the symmetric part of e_{ijk} contributes to the electromechanical energy. Consequently, the physically relevant piezoelectric tensor must satisfy $e_{ijk} = e_{ikj}$, which reduces the number from 27 to 18 independent components.

Because the PZT disc is assumed to be transversely isotropic (6 mm symmetry), with its symmetry axis along the $z = x_3$ direction, the piezoelectric tensor reduces from 18 independent components to only three. In Voigt notation, the non-zero components are conventionally written as $e_{31} = e_{311} = e_{322}$ (transverse coupling), $e_{33} = e_{333}$ (axial coupling), and $e_{15} = e_{113} = e_{223}$ (shear coupling). Moreover, the constitutive relations in (9) become

$$\boldsymbol{\sigma}_V = \mathbf{C}^E_V\,\boldsymbol{\epsilon}_V - \mathbf{e}^T\boldsymbol{E}, \quad \boldsymbol{D} = \mathbf{e}\,\boldsymbol{\epsilon}_V + \boldsymbol{\varepsilon}^{\epsilon}\,\boldsymbol{E}, \tag{10}$$

where

$$\mathbf{e} = \begin{bmatrix} 0 & 0 & 0 & 0 & e_{15} & 0 \\ 0 & 0 & 0 & e_{15} & 0 & 0 \\ e_{31} & e_{31} & e_{33} & 0 & 0 & 0 \end{bmatrix} \tag{11}$$

is the piezoelectric coupling matrix. Here $\boldsymbol{E} = [E_1\ E_2\ E_3]^T$ and $\boldsymbol{D} = [D_1\ D_2\ D_3]^T$. We can write (10) in matrix form as

$$\begin{bmatrix} \boldsymbol{\sigma}_V \\ \boldsymbol{D} \end{bmatrix} = \mathbf{M} \begin{bmatrix} \boldsymbol{\epsilon}_V \\ \boldsymbol{E} \end{bmatrix}, \quad \mathbf{M} = \begin{bmatrix} \mathbf{C}_V & -\mathbf{e}^T \\ \mathbf{e} & \boldsymbol{\varepsilon} \end{bmatrix}. \tag{12}$$

The coupling matrix $\mathbf{M}$ is a 9×9 matrix.

Following the UEIS formulation [20], the piezoelectric coefficients were treated as real-valued, $e_{ij} = e'_{ij} + 0\mathrm{i}$. This assumption is consistent with low-frequency measurements [24], although its validity near megahertz thickness-mode resonances must be assessed carefully [20]. In the RP-UEIS fits, trial optimizations including $\mathrm{Im}[e_{ij}]$ showed negligible spectral sensitivity to these parameters. Their inclusion produced overfitting: the global error decreased only marginally, while the agreement at the critical resonance minimum, $Z_{\min}$, deteriorated. The measured spectra were therefore adequately described by mechanical and dielectric losses, justifying real-valued piezoelectric coefficients and improving the stability and interpretability of the inverse problem.

For passive PZT materials, the power-dissipation density must be non-negative for any admissible stress–strain and electric-field configuration. In Appendix, we examine the implications of this passivity requirement for the constitutive tensors, with particular attention to the stiffness coefficients. From this analysis, the following constraints are obtained:

$$C''_{12} \geq C''_{11}, \quad C''_{44} \leq 0, \quad C''_{66} \leq 0, \quad \varepsilon''_{11} \geq 0, \quad \varepsilon''_{33} \geq 0, \tag{13a}$$

$$C''_{11} + C''_{12} + C''_{33} \leq -\sqrt{R}, \tag{13b}$$

where

$$R = C''^{\,2}_{11} + 2C''_{11}C''_{12} - 2C''_{11}C''_{33} + C''^{\,2}_{12} - 2C''_{12}C''_{33} + 8C''^{\,2}_{13} + C''^{\,2}_{33}. \tag{14}$$

These constraints will be incorporated into the optimization procedure used to extract the material parameters from the electrical-impedance measurements of PZT ceramics. Note that we have dropped the superindex ^{E} of the stiffness coefficients for simplicity.

Finally, we neglect dielectric loss in the transverse direction, i.e. we set $\varepsilon''_{11} = 0$. This simplification is justified both experimentally and geometrically: in a poled PZT ceramic driven in thickness mode, the electric field is strictly aligned with the poling axis and the measured response is therefore sensitive only to the longitudinal permittivity ε_{33}. Any transverse dielectric loss ε''_{11} does not enter the governing equations and cannot be identified from the frequency response.

Considering the constitutive relations in (10) and our previous discussions here, we find the total number of independent parameters to describe a PZT ceramic material is sixteen. These parameters, with their respective value, are summarized in Table 1.

2.4. Fluid model

The coupling gel layer between the PZT disc and the test material (or acoustochip) is modeled as a thin water-like layer of thickness d, whose role is to efficiently transmit acoustic energy from the PZT into the adjacent polymeric layers. The internal cavity of the acoustochip is represented as a cylindrical domain of height h_c and radius r_c, filled with a lossless fluid. Under these assumptions, the acoustic pressure field p in each fluid domain satisfies the homogeneous Helmholtz equation,

$$\left(\nabla^2 + k_f^2\right)p = 0, \tag{15}$$

Table 1
Nominal PZT-4 material parameters relevant to the RP-UEIS model, as implemented in COMSOL Multiphysics software.

Category	Symbol	Value
Stiffness		
Real part (GPa)	C'_{11}	138.99
	C'_{12}	77.84
	C'_{13}	74.28
	C'_{33}	115.41
	C'_{44}	25.64
Imaginary part	$C''_{11}, C''_{12}, C''_{13}, C''_{33}, C''_{44}$	Not available
Piezoelectric constants		
$(\mathrm{C\,m^{-2}})$	e'_{31}	−5.2
	e'_{33}	15.08
	e'_{15}	12.72
Permittivity		
Real part	ε'_{11}	762.5
	ε'_{33}	663.2
Imaginary part	ε''_{33}	Not available
Number of parameters		16

where $k_\mathrm{f} = \omega/c_\mathrm{f}$ is the wavenumber and c_f is the speed of sound in the medium. The fluid velocity is given by

$$\boldsymbol{v} = \frac{\mathrm{i}}{\rho_\mathrm{f}\omega}\boldsymbol{\nabla}p, \tag{16}$$

where ρ_f is the fluid density.

At all solid–fluid interfaces, the acoustic and elastic fields are coupled through continuity of normal displacement and normal stress, ensuring proper transfer of acoustic energy between the PZT disc, the polymeric structure, and the fluid-filled cavity.

2.5. Polymer materials

The polymer layers that form the acoustochip, serving as substrate, sidewalls, and adhesive interfaces, are modeled as linear, isotropic, and homogeneous viscoelastic solids. Under time-harmonic deformation fields of the form $\mathrm{e}^{-\mathrm{i}\omega t}$, the constitutive relation for an isotropic medium is written in terms of the stress and strain amplitude tensors as

$$\sigma_{ij} = \left(K - \frac{2G}{3}\right)\epsilon_{kk}\,\delta_{ij} + 2G\,\epsilon_{ij}, \tag{17}$$

where δ_{ij} is the Kronecker delta symbol, $K = K' + \mathrm{i}K''$ and $G = G' + \mathrm{i}G''$ denote the complex-valued adiabatic bulk and shear moduli, respectively. The real and imaginary parts of K and G account, respectively, for energy storage and dissipation associated with bulk and shear deformation.

Assuming that low-amplitude ultrasonic plane waves propagate within the polymer layers, we introduce the longitudinal and shear complex wavenumbers as $k_\mathrm{l} = k'_\mathrm{l} + \mathrm{i}\alpha_\mathrm{l}$ and $k_\mathrm{s} = k'_\mathrm{s} + \mathrm{i}\alpha_\mathrm{s}$. These wavenumbers define the corresponding phase velocities and ultrasonic absorption coefficients through

$$c_\mathrm{l} = \frac{\omega}{k'_\mathrm{l}} = \sqrt{\frac{K' + 4G'/3}{\rho_\mathrm{s}}}, \quad c_\mathrm{s} = \frac{\omega}{k'_\mathrm{s}} = \sqrt{\frac{G'}{\rho_\mathrm{s}}}, \tag{18a}$$

$$\alpha_\mathrm{l} = \frac{k'_\mathrm{l}}{2}\tan\delta_\mathrm{l}, \quad \alpha_\mathrm{s} = \frac{k'_\mathrm{s}}{2}\tan\delta_\mathrm{s}, \tag{18b}$$

in which ρ_s is the solid density. Here we adopt the weak-absorption approximation, under which the viscoelastic losses are small. This leads to the loss tangents $\tan\delta_\mathrm{l} = (K'' + 4G''/3)/(K' + 4G'/3) \ll 1$ and $\tan\delta_\mathrm{s} = G''/G' \ll 1$. In the case of purely elastic solids, the loss tangents are set to zero, i.e., no ultrasonic absorption takes place in the associated medium.

By introducing the complex-valued bulk and shear moduli, the model acquires four additional material parameters. With these additions, the total number of independent parameters in the description temporarily increases to twenty. This parameter set will later be reduced by performing a sensitivity analysis within the optimization space to identify and retain only those parameters to which the model response is significantly sensitive.

2.6. Boundary conditions

We restrict our analysis to PZT discs of radius a and height h. A cylindrical coordinate system (r, φ, z) is set at the center of the disc bottom surface. The applied voltage excitation generates axisymmetric electromechanical fields with respect to the PZT disc axis of symmetry $(r = 0)$. As a consequence, the displacement field is independent of the azimuthal coordinate and can be written as $\boldsymbol{u}(r, z)$.

For a PZT disc with free lateral and bottom surfaces, as shown in Fig. 1(a), the mechanical boundary condition is

$$\boldsymbol{\sigma}\cdot\boldsymbol{n} = \boldsymbol{0}, \qquad \text{on the free boundaries,} \tag{19}$$

where $\boldsymbol{n}$ denotes the outward unit normal vector. Also, assuming that the PZT disc is electrically insulated, no free electric charge can cross its boundaries. Therefore, the normal component of the electric displacement vanishes,

$$\boldsymbol{D}\cdot\boldsymbol{n} = 0, \qquad \text{on the insulated boundaries.} \tag{20}$$

An important electromagnetic quantity in the characterization of PZT ceramics is the electric current density $\boldsymbol{J}$. In dielectric materials, this current arises from the time variation of the polarization field $\boldsymbol{P}$, representing the net motion of electric dipole moments per unit volume. Thus, $\boldsymbol{J} = \partial_t\boldsymbol{P}$. Using the constitutive relation for polarizable media, $\boldsymbol{D} = \varepsilon_0\boldsymbol{E} + \boldsymbol{P}$, (with ε_0 being the electric permittivity of free space). and adopting the time-harmonic convention $\partial_t = -\mathrm{i}\omega$, we obtain

$$\boldsymbol{J} = -\mathrm{i}\omega\boldsymbol{P} = -\mathrm{i}\omega\left(\boldsymbol{D} - \varepsilon_0\boldsymbol{E}\right). \tag{21}$$

The total electric current I passing through a PZT disc of radius a is obtained by integrating the axial current density component J_3 over the electrode top area,

$$I = -2\pi\int_0^a J_z(r,h)\,r\,\mathrm{d}r = -2\pi\,\mathrm{i}\omega\left(\varepsilon_{33} - \varepsilon_0\right)\int_0^a E_z(r,h)\,r\,\mathrm{d}r. \tag{22}$$

This current is excited by an applied electric potential difference $\Delta V\,\mathrm{e}^{-\mathrm{i}\omega t}$, with $\Delta V = V_2 - V_1$ being the potential amplitude, across the bottom and top PZT surfaces. The resulting electrical impedance of the PZT disc is therefore defined as $Z = \Delta V/I$.

Consider a coupling-gel (liquid) layer of thickness d inserted between the top surface of the PZT disc and the polymer sample, as illustrated in Fig. 1(b). At each solid–liquid interface, continuity of the normal kinematics and traction must be enforced. These conditions read

$$\boldsymbol{v}\cdot\boldsymbol{n} = -i\omega\,\boldsymbol{u}\cdot\boldsymbol{n}, \quad \boldsymbol{\sigma}\cdot\boldsymbol{n} = -p\,\boldsymbol{n}, \quad \text{on solid–liquid interfaces.} \tag{23}$$

Moreover, a pressure-release condition is imposed,

$$p = 0, \qquad \text{on lateral fluid boundaries.} \tag{24}$$

Fig. 1(c) illustrates the cross-sectional representation of a multilayer acoustochip. At each material interface, continuity conditions for the relevant physical fields must be satisfied. The external boundaries are assigned the same boundary conditions described for Figs. 1(a) and (b).

3. Methods and materials

3.1. Custom RP-UEIS system

The experimental setup developed for the RP-UEIS in both unloaded and coupled material setup is shown in Fig. 2. The measurement circuit consists of a low-inductance reference resistor of $R = 0.5\ \Omega$ connected in series with a PZT-4 disc (Eleceram Technology Co., Ltd., China) of diameter $2a = 25\,\mathrm{mm}$, thickness $h = 2.02\,\mathrm{mm}$, and density

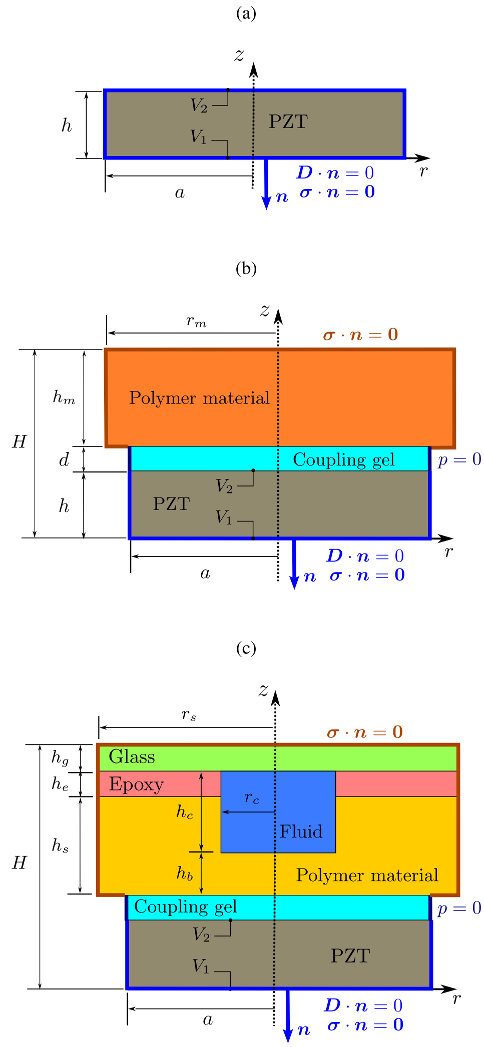

Fig. 1. Two-dimensional cross-sectional representations of the modeled configurations and associated boundary conditions. (a) Isolated PZT disc used for the initial electromechanical characterization. (b) RP-UEIS configuration consisting of the PZT disc coupled through a thin gel layer to a solid material under test. (c) Acoustochip with a central fluid-filled cavity, an epoxy bonding layer, and a glass superstrate.

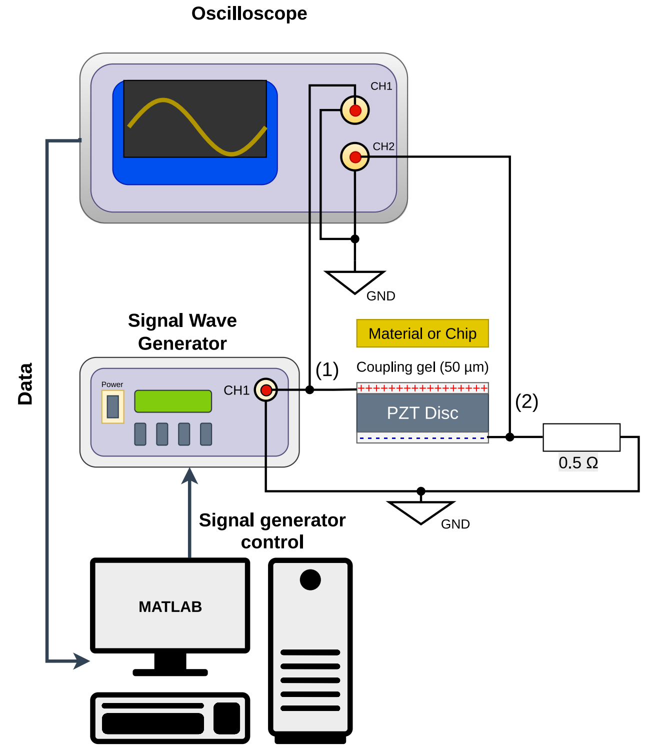

Fig. 2. Custom ultrasonic electrical impedance spectroscopy (UEIS) setup. (1) Excitation voltage; (2) Voltage across the series reference resistor. The system integrates Matlab-based signal generator control and oscilloscope data acquisition.

$7862\,\mathrm{kg\,m^{-3}}$. The nominal resonance frequency of the PZT-4 disc is $f_0 = 1\,\mathrm{MHz} \pm 5\%$. To ensure experimental reproducibility and evaluate manufacturing tolerances, four identical discs from this commercial batch were initially characterized under identical conditions. The experimental repeatability was excellent, exhibiting a maximum dispersion in their baseline resonance frequencies of only 0.19 % (ranging from 1033.44 kHz to 1035.45 kHz), alongside highly consistent impedance profiles. Consequently, for the sake of conciseness and graphical clarity in the multi-parameter curves, a single representative PZT disc was selected to present the detailed RP-UEIS parameter identification process throughout this work.

Two electrical signals were monitored during the measurements: (i) the excitation voltage applied to the circuit, corresponding to the output of the function generator (FY3200S, Feeltech, China), which also served as the oscilloscope (TDS 2024B, Tektronix, Inc., USA) trigger; and (ii) the voltage across the series reference resistor, measured with a passive oscilloscope probe connected directly across its terminals to minimize parasitic cable reactance. The PZT disc voltage was calculated as the difference between these two signals. Since the voltage drop across the reference resistor was negligible compared with that across the PZT disc, the excitation voltage provided an excellent approximation of the PZT disc voltage, which varied with the acoustic load. To ensure a sufficient number of steady-state cycles were captured for spectral analysis, the oscilloscope time base was set to $2.5\,\mathrm{\mu s/div}$. All voltage signals are recorded simultaneously using the oscilloscope and subsequently transferred to a computer for post-processing and impedance evaluation in Matlab (Mathworks, Inc., USA), which also controls the function generator.

To obtain the impedance spectrum, a continuous sinusoidal excitation with a $5.0\,\mathrm{V_{pp}}$ amplitude is applied at a sequence of discrete frequencies. The sweep covers a range of $\pm 12\%$ around the nominal resonance frequency f_0, with a frequency step of $\Delta f = 500\,\mathrm{Hz}$. The total duration of this characterization procedure is approximately 13.33 min. For each excitation frequency, the measured voltage signals are post-processed by computing their fast Fourier transforms (FFT), from which the amplitude and phase of the steady-state response at the driving frequency are extracted. The complex impedance is then computed as

$$Z(\omega) = \frac{\Delta V(\omega)}{I(\omega)} = \frac{\Delta V(\omega)}{\Delta V_{\mathrm{R}}(\omega)} R, \tag{25}$$

where $\Delta V_{\mathrm{R}}(\omega)$ denotes the voltage amplitude across the reference resistor.

3.2. Finite element modeling

The physical models of the PZT disc, in both unloaded and loaded configurations, are implemented in Comsol Multiphysics Finite-element analysis (FEA) software (COMSOL AB, Sweden). The governing equations of motion and electrostatics, given by Eqs. (4) and (8), together with the boundary and continuity conditions described in Section 2.6, are solved in the frequency domain using a coupled multiphysics framework.

The simulations employ the `Structural Mechanics Module` to describe the elastic and piezoelectric response of the solid domains, the `AC/DC Module` to model the quasistatic electric field in the PZT disc, and the `Acoustics Module` to represent the pressure field in the fluid domains, when present.

The RP-UEIS method consists of three algorithms: sensitivity analysis, parameter identification of the PZT disc, and parameter identification of the test sample. These algorithms are implemented in MATLAB, interfaced with `LiveLink for MATLAB` in COMSOL.

To ensure numerical accuracy, a mesh sensitivity analysis was performed for all FEA models. The domains were discretized using second-order elements, with the maximum element size restricted to $\lambda_{\min}/10 \approx 0.123\,\mathrm{mm}$. This minimum wavelength ($\lambda_{\min} \approx 1.23\,\mathrm{mm}$) was calculated using the speed of sound in water ($c = 1480\,\mathrm{m\,s^{-1}}$), which represents the medium with the lowest propagation velocity in the system, evaluated at the highest operating frequency ($1.2\,\mathrm{MHz}$) to properly resolve acoustic wave propagation. Local mesh refinement was applied in critical regions such as the thin coupling gel layer and solid–fluid interfaces. The mesh was progressively refined until the relative variation in resonance frequency and minimum impedance magnitude between consecutive refinements was below $3\,\%$.

All simulations and inverse optimization routines were executed on a laptop equipped with an AMD Ryzen 5 5500U processor (2.10 GHz) and 16 GB RAM. The initial sensitivity analysis for the PZT-4 disc required approximately 30 min. The inverse fitting of the piezoelectric parameters converged in about 4 h, while the viscoelastic parameter extraction for each polymer sample required 50 min.

3.3. Sensitivity analysis of PZT parameters

To identify the most influential piezoelectric parameters governing the electrical response of the PZT disc, a local sensitivity analysis is performed around the nominal parameter vector within the framework of an inverse problem. In such problems, parameter identifiability and robustness of the solution are strongly influenced by the sensitivity of the model response to perturbations in the parameter space [22,25].

The objective here is to quantify how small perturbations in each material parameter affect the simulated impedance spectrum and to determine which parameters should be retained in the inverse optimization procedure. The sensitivity analysis is based on finite-element simulations of the PZT disc, from which the complex electrical impedance $Z_m^{\mathrm{num}} = Z^{\mathrm{num}}(f_m;\theta)$ and admittance $Y_m^{\mathrm{num}} = \left[Z^{\mathrm{num}}(f_m;\theta)\right]^{-1}$ are computed at the discrete frequency f_m ($m = 1, 2, \dots, M$) for a prescribed complex parameter vector $\theta = \theta' + \mathrm{i}\theta''$, where θ' and θ'' denote, respectively, the real and imaginary parts of the parameter vector. The reference responses, corresponding to the nominal parameter vector provided by the manufacturer, $\theta_0 = \theta_0' + \mathrm{i}\theta_0''$, are denoted by Z_m^{ref} and Y_m^{ref}.

To quantify the influence of individual material parameters, the residuals between the reference and simulated frequency responses are defined as

$$R_m^{\mathrm{mag}} = \begin{cases} \log\left|Z_m^{\mathrm{ref}}\right| - \log\left|Z_m^{\mathrm{num}}\right|, & \text{varying } \theta', \\ \left|Y_m^{\mathrm{ref}}\right| - \left|Y_m^{\mathrm{num}}\right|, & \text{varying } \theta''. \end{cases} \tag{26}$$

The logarithmic formulation of the impedance magnitude is adopted when perturbing the real part (θ') of the parameter vector, in order to measure relative deviations between the reference and simulated responses. Since the impedance spectrum of a resonant PZT disc typically spans several orders of magnitude between resonance and antiresonance, the logarithm compresses the dynamic range and improves numerical conditioning, while preventing high-magnitude peaks from dominating the residual. In contrast, when perturbing the imaginary part (θ'') of the parameter vector the residual is defined in terms of the admittance magnitude. Loss-related parameters primarily influence damping and peak broadening, which are more directly and sensitively reflected in the admittance response near resonance. This combined strategy enhances parameter identifiability and balances sensitivity across stiffness- and dissipation-dominated effects.

The residuals are stacked into a single vector $\mathbf{R}$:

$$\mathbf{R} = \left[R_1^{\mathrm{mag}}, \dots, R_M^{\mathrm{mag}}\right]^T. \tag{27}$$

Hence, the cost function is defined as the squared Euclidean norm of this residual vector:

$$C = \mathbf{R}^T\mathbf{R}. \tag{28}$$

The sensitivity analysis is formulated by examining the local response of the cost function (defined in Eq. (28)) to individual perturbations of the material parameter vector θ_0. The reference impedance Z_m^{ref} is obtained from the finite-element forward model using θ_0. A family of perturbed parameters are then generated as

$$\theta_{ij}^{\mathrm{real}} = (\theta_{0,1}, \dots, \alpha_j\,\theta_{0,i}' + \mathrm{i}\theta_{0,\mathrm{i}}'', \dots, \theta_{0,N_p}), \tag{29a}$$

$$\theta_{ij}^{\mathrm{imag}} = (\theta_{0,1}, \dots, \theta_{0,i}' + \mathrm{i}\alpha_j\,\theta_{0,\mathrm{i}}'', \dots, \theta_{0,N_p}), \tag{29b}$$

where $N_p = 16$ is the number of PZT parameters and $\alpha_j = 0.7 + 0.6(j-1)/(N_s-1)$ ($j = 1, 2, \dots, N_s$) is a scaling factor, with $N_s = 50$ being the number of scaling points.

For each parameter variation described in Eq. (29), a scalar sensitivity index s_i is defined as

$$s_i = \max_j \left|\frac{c_{i,j+1} - c_{ij}}{\alpha_{j+1} - \alpha_j}\right|, \tag{30}$$

where $c_{ij} = C(\theta_{ij})$, with θ_{ij} being either $\theta_{ij}^{\mathrm{real}}$ or $\theta_{ij}^{\mathrm{imag}}$. The PZT parameters are subsequently ranked according to decreasing s_i, providing a quantitative measure of their influence on the modeled impedance response. In Algorithm 1, we illustrate the complete procedure handling both parameter types.

Algorithm 1 Sensitivity analysis of PZT disc material parameters.

Require: Baseline parameter names and values $\left\{Name_i, \theta_{0,i}\right\}_{i=1}^{N_p}$ and frequency set $\{f_m\}_{m=1}^{N_f}$
Ensure: Sensitivity ranking table $\mathbf{T}$

```
Compute {Z_m^ref(θ_0)}_{m=1}^{M} via FEM
Define α = {α_j}_{j=1}^{N_s} with α_j = 0.7 + 0.6(j − 1)/(N_s − 1)
for i = 1 to N_p do
    Set θ ← θ_0
    for j = 1 to N_s do
        Compute Z_ij^real = {Z_m^num(θ_ij^real)}_{m=1}^{M} and Z_ij^imag = {Z_m^num(θ_ij^imag)}_{m=1}^{M} via FEM
        Compute c_ij^real = C(Z_ij^real) and c_ij^imag = C(Z_ij^imag)    ▷ from Eq. (28)
    end for
    Compute s_i^real and s_i^imag using Eq. (30)
end for
Build ranking table and sort:
    T ← Sort({(Name_i, s_i^real, s_i^imag)}_{i=1}^{N_p}, }}descendε)
return T
```

The sensitivity coefficient s_i was evaluated for the PZT-4 disc. Table 2 lists the PZT-4 parameters together with their corresponding normalized sensitivity values s_i, ordered in descending magnitude. It is worth noting that, as established in the theoretical framework (Section 2.3), the imaginary components of the piezoelectric coefficients ($\mathrm{Im}[e_{ij}]$) were deliberately excluded from this sensitivity ranking and the subsequent optimization space, as their unidentifiability would needlessly risk ill-conditioning the inverse problem.

Thresholds of 10% and 30% relative to the maximum sensitivity slope were adopted for the real and imaginary components of the PZT parameters, respectively. Parameters with sensitivities below these

Table 2
Ranking table of the sensitivity analysis of PZT-4 based on the slope of the cost function near zero variation.

Real Part		Imaginary Part	
Parameter	Slope	Parameter	Slope
C'_{33}	1.000	C''_{33}	1.000
C'_{11}	0.564	C''_{11}	0.539
C'_{13}	0.462	C''_{13}	0.442
C'_{44}	0.331	–	–
e'_{33}	0.305	–	–
ε'_{33}	0.178	–	–
e'_{15}	0.121	–	–

Number of parameters: 10.

levels were found to have a negligible influence on the modeled response and are therefore weakly observable from the measurements. Note that separate thresholds were adopted for the real and imaginary components because they influence different spectral features: primarily resonance location and damping, respectively. They are evaluated using different residual metrics. The selected values correspond to the smallest cutoffs that provided stable convergence of the inverse procedure and accurate reconstruction of the measured impedance spectrum. Applying these selection criteria results in a reduction of the optimization space from 16 to 10 independent variables, specifically 7 real and 3 imaginary coefficients. This dimensionality reduction strategy constitutes the basis of the RP-UEIS method proposed in this work. Regarding the parameters excluded from the optimization, the insensitive real coefficients are fixed at their nominal values, while the negligible imaginary components are set to zero.

3.4. PZT parameters estimation

The PZT parameters are identified using the RP-UEIS strategy with the reduced set of 10 most sensitive parameters determined in the sensitivity analysis (Algorithm 2). The problem is formulated as a nonlinear inverse optimization in which the parameter vector $\boldsymbol{\theta}$ is iteratively updated to minimize the cost function defined in Eq. (28). The resonance frequency f_0 is first estimated from the minimum of the measured impedance magnitude. A frequency window of $\pm 12\%$ around f_0 is then selected, and only the spectral data within this range are used in the optimization to focus on the dominant thickness-mode response.

Starting from the nominal parameter set θ_0, the parameter estimation proceeds in a block-wise manner using the Nelder–Mead simplex algorithm implemented using the `fminsearch` routine in Comsol Multiphysics software. First, the storage elastic coefficients $\boldsymbol{\theta}_A = [C'_{11}, C'_{13}, C'_{33}, C'_{44}]$ are optimized using the logarithmic impedance metric. Next, the storage piezoelectric and dielectric parameters $\boldsymbol{\theta}_B = [e'_{15}, e'_{33}, \varepsilon'_{33}]$ are refined, while the remaining insensitive real parameters are kept fixed. The loss parameters are then estimated using the reduced subset $\theta_C = [C''_{11}, C''_{13}, C''_{33}]$, with all other imaginary components set to zero. This stage employs the admittance-based metric and constrained minimization via `fminsearchcon` routine in Comsol Multiphysics software to enforce the energetic consistency condition of Eq. (13a). After each block update, the forward model is re-evaluated. The iterations terminate when the relative variation of the cost function falls below 5%, ensuring convergence to a locally consistent parameter set.

3.5. Parameter estimation of polymer materials

To estimate the viscoelastic parameters of a sample attached to the PZT disc through a coupling gel layer, we adopt a procedure analogous to that described in Algorithm 2. The optimization is consolidated into a single fitting stage focused entirely on the sample parameter vector $\boldsymbol{\theta}_\mathrm{S} = [K', K'', G', G'']$, representing the storage and loss components of

Algorithm 2 RP-UEIS method for determining the PZT disc parameters.

Require: Experimental spectrum $\{f_m, Z_m^{\mathrm{exp}}\}_m^M$, and nominal PZT parameter vector $\boldsymbol{\theta}_0$
Ensure: Identified reduced PZT parameter set $\boldsymbol{\theta}$
Set the resonance frequency: $f_0 \leftarrow \arg\left(\min_m |Z_m^{\mathrm{exp}}(f_m)|\right)$
Set $\boldsymbol{\theta} \leftarrow \boldsymbol{\theta}_0$
$C_{\mathrm{ref}} \leftarrow C(\boldsymbol{\theta})$
Set err $\leftarrow 1$
Iter $\leftarrow 0$
Select data subsets with $f_m \in \Delta f$
while err ≥ 0.05 **do**
    Iter $\leftarrow$ Iter $+ 1$
    if Iter $= 1$ **then**
        Define a frequency window Δf centered at f_0 with $\pm 3\%$ bandwidth
    else
        Define a frequency window Δf centered at f_0 with $\pm 12\%$ bandwidth
    end if
    Compute $Z_m^{\mathrm{num}}(\boldsymbol{\theta})$ and $Y_m^{\mathrm{num}}(\boldsymbol{\theta})$ via FEM
    $\boldsymbol{\theta}_\mathrm{A} \leftarrow [C'_{11}, C'_{13}, C'_{33}, C'_{44}]$ ▷ Stage A
    $\boldsymbol{\theta}_\mathrm{A}^* \leftarrow \arg\left[\min_{\boldsymbol{\theta}_\mathrm{A}} C(\boldsymbol{\theta})\right]$ via `fminsearch`
    Update $\boldsymbol{\theta} \leftarrow (\boldsymbol{\theta} \setminus \boldsymbol{\theta}_\mathrm{A}) \cup \boldsymbol{\theta}_\mathrm{A}^*$
    $\boldsymbol{\theta}_\mathrm{B} \leftarrow [e'_{15}, e'_{33}, \varepsilon'_{33}]$ ▷ Stage B
    $\boldsymbol{\theta}_\mathrm{B}^* \leftarrow \arg\left[\min_{\boldsymbol{\theta}_\mathrm{B}} C(\boldsymbol{\theta})\right]$ via `fminsearch`
    Update $\boldsymbol{\theta} \leftarrow (\boldsymbol{\theta} \setminus \boldsymbol{\theta}_\mathrm{B}) \cup \boldsymbol{\theta}_\mathrm{B}^*$
    $\boldsymbol{\theta}_\mathrm{C} \leftarrow [C''_{11}, C''_{13}, C''_{33}]$ ▷ Stage C
    $\boldsymbol{\theta}_\mathrm{C}^* \leftarrow \arg\left[\min_{\boldsymbol{\theta}_\mathrm{C}} C(\boldsymbol{\theta})\right]$ via `fminsearchcon`
    subject to constraint given in Eq. (13)
    Update $\boldsymbol{\theta} \leftarrow (\boldsymbol{\theta} \setminus \boldsymbol{\theta}_\mathrm{C}) \cup \boldsymbol{\theta}_\mathrm{C}^*$
    $C \leftarrow C(\boldsymbol{\theta})$
    err $\leftarrow |C - C_{\mathrm{ref}}|/|C_{\mathrm{ref}}|$
    $C_{\mathrm{ref}} \leftarrow C$
end while
return $\boldsymbol{\theta}$

the bulk and shear moduli. To accurately capture these parameters, this stage uses the narrow frequency window of $\pm 10\%$ around f_0. Given the significant damping introduced by the viscoelastic material, the cost function is strictly defined using the admittance-based residuals. This metric provides superior sensitivity to the broadening of the resonance peaks caused by the material losses. Finally, to ensure physical admissibility during the minimization, all components of $\boldsymbol{\theta}_\mathrm{S}$ are constrained to be strictly positive, and an additional nonlinear constraint is imposed on the real part of the Poisson's ratio (ν), to maintain it within a realistic range for the characterized material.

3.6. Polymer material preparation and testing

Five representative polymeric materials were selected as test samples: PLA, ABS, PET-G, PMMA and epoxy resin. All samples were prepared in the form of circular discs with a diameter of 26 mm and 1 mm thickness. The mass density of each material (ρ_s) was determined experimentally by measuring the sample mass with an analytical balance (ME204, Mettler Toledo, USA) and computing the volume from its geometric dimensions.

The fabrication methods were adapted according to the material type. The thermoplastic specimens (PLA, ABS, and PET-G) were fabricated using fused deposition modeling (FDM) with a commercial 3D printer (X1 Carbon, Bambu Labs, China). To ensure optimal layer adhesion and minimize thermal residual stresses, the nozzle and build plate temperatures were individually optimized for each polymer in

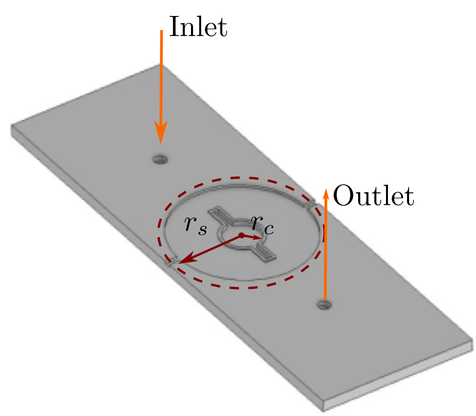

Fig. 3. Three-dimensional computer-aided rendering of the PLA substrate for the acoustochip, illustrating the central fluidic cavity and the inlet and outlet ports. The red dashed circle, defined by the radius r_s, delimits the active region extracted for the 2D axisymmetric numerical model, and r_c is the cavity radius.

accordance with the filament manufacturer's specifications. In contrast, the PMMA samples were obtained from a commercial cast acrylic sheet with a thickness of 1 mm. In this case, the specimens were machined into the required disc geometry using a laser cutting system (NCRL6040P, Nagano, China). The epoxy samples (two-component adhesive Araldite Professional, Tekbond, Brazil) were produced by casting the resin into a cylindrical mold of the same dimensions as previously described. After casting, the mold was placed in a degassing chamber for 1 h to eliminate air bubbles. The resin was then allowed to cure at room temperature for 24 h.

Prior to the impedance measurements, the contact surface of each polymer disc was polished using 800-grit sandpaper to remove any manufacturing irregularities and ensure a uniform acoustic interface. Subsequently, each sample was bonded to the surface of the PZT-4 disc using a thin layer of commercial ultrasonic coupling gel. After assembly, the thickness of the coupling gel layer was measured to be approximately 20 μm.

3.7. Acoustochip fabrication and experimental setup

To validate the applicability of the RP-UEIS approach to multilayer polymer-based acoustofluidic devices, a representative acoustochip was fabricated and experimentally characterized. The device consists of a layered assembly comprising a PZT-4 disc, a 3D-printed PLA substrate incorporating the fluidic structure, an epoxy bonding layer, and a glass superstrate acting as an acoustic reflector (Fig. 3). The central element is a circular microcavity designed to support a half-wavelength ($\lambda/2$) standing wave in water at approximately 1 MHz.

To experimentally confirm the formation of the acoustic standing wave, a suspension of 10 μm polystyrene microbeads was introduced into the cavity. The PZT disc was driven at 10 V_{pp} using a function generator (FY3200S, Feeltech, China) to induce the acoustic radiation force-mediated particle aggregation at the pressure node in the cavity's midheight. The resulting particle pattern was observed with an upright optical microscope (k55-BA, Olen, China) equipped with a 4K digital camera (Eakins, China).

4. Results and discussion

4.1. Measurements with a commercial impedance analyzer

We compare the impedance data measured using the custom RP-UEIS system with those obtained from a commercial impedance analyzer (HF2IS, Zurich Instruments, Switzerland). The measured impedance spectra shown in Fig. 4 are in good agreement, with both systems identifying the fundamental resonance at f_0 = 1.03 MHz. The mean absolute percentage error (MAPE) between the datasets is approximately 10% over the analyzed frequency range. The remaining differences are likely due to resistor tolerances and contact resistance, oscilloscope sampling and gain uncertainties, and slight variations in loading conditions between the two setups.

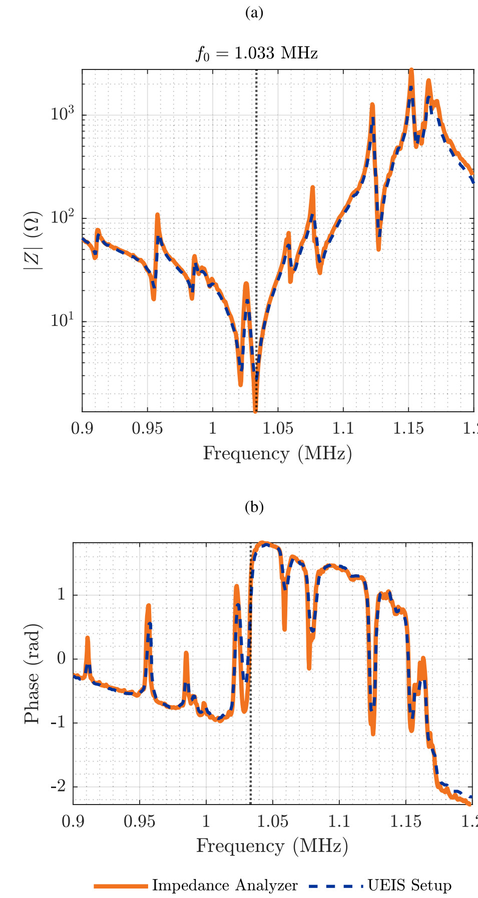

Fig. 4. Benchmarking of the experimental impedance spectra obtained using the custom RP-UEIS setup versus the commercial impedance analyzer (HF2IS). (a) Impedance magnitude and (b) phase spectra. The MAPE of the impedance magnitude is 10%.

4.2. PZT-4 disc parameters

The electromechanical parameters of the PZT-4 disc were identified using the RP-UEIS method detailed in Section 3.4. Given that standard commercial datasheets typically omit dissipative coefficients, the imaginary stiffness components (C''_{11}, C''_{13}, and C''_{33}) were undetermined. To establish a starting point for the optimization, these were initialized as a fixed fraction of the real part: $C''_{ij} = 0.001C'_{ij}$.

Table 3 lists the ten optimized parameters together with their nominal manufacturer values. For the real-valued parameters, the largest relative deviation remains below 15%. In contrast, the imaginary parameters may require further adjustments, indicating that the initially assumed damping was significantly underestimated. The material constants obtained with the RP-UEIS method show good agreement with values reported in the literature. The real elastic stiffness C'_{33} = 121.67 GPa lies within the typical range reported for hard PZT materials and is consistent with the stiffness magnitudes identified by using Resonant Ultrasound Spectroscopy (140–640 kHz) [26]. Minor deviations in C'_{11}, C'_{13}, and e'_{33} (all below 10%) are likewise within the

Table 3
Nominal θ_0 and fitted θ parameters of the PZT-4 disc obtained with the RP-UEIS method. The percentage difference is calculated relative to the nominal values.

Parameter	Nominal	Fitted	Units	Difference (%)
C'_{11}	138.99	137.00	GPa	−1.43
C'_{13}	74.28	77.46	GPa	4.27
C'_{33}	115.41	121.67	GPa	5.42
C'_{44}	25.64	22.00	GPa	−14.21
e'_{15}	12.72	13.05	$\mathrm{C\,m^{-2}}$	2.59
e'_{33}	15.08	16.56	$\mathrm{C\,m^{-2}}$	9.81
ε'_{33}	663.20	753.87	–	13.67
C''_{11}	−0.14	−0.08	GPa	−44.60
C''_{13}	0.07	0.11	GPa	45.95
C''_{33}	−0.12	−0.30	GPa	161.74

variability expected between identification techniques. Furthermore, the imaginary stiffness components accurately reflect the dynamic behavior of the PZT disc under high-frequency excitation. From the fitted parameters, the elastic dissipation factor is $|C''_{33}|/C'_{33} \approx 2.5 \times 10^{-3}$. This value is in excellent agreement with recent high-frequency characterizations of hard PZT materials, aligning precisely with the parameters extracted by Kar et al. [27] for PZT discs and by Bodé et al. [20] using ultrasound electrical-impedance spectroscopy in the megahertz range. This consistency confirms the physical validity of the characterized free PZT disc model, establishing a reliable baseline for the subsequent extraction of the polymer's viscoelastic properties.

In Fig. 5, the electrical impedance spectra are presented for the experimental measurements, the nominal (unfitted) model, and the optimized (fitted) model. A clear improvement is observed after optimization, with the fitted response closely tracking both the magnitude and phase behavior of the experimental data. The MAPE between the fitted model and the measurements remains below 22.4% over the analyzed frequency range.

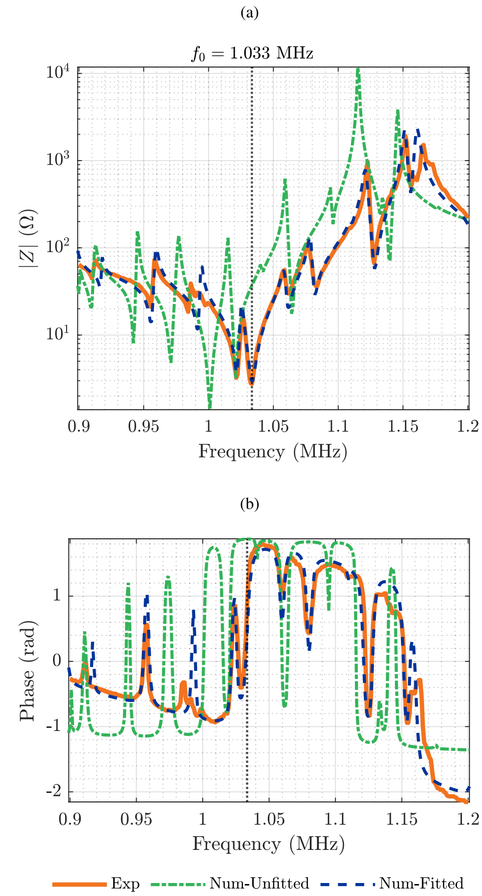

Fig. 5. Experimental validation of the RP-UEIS fitting procedure for the PZT-4 disc. (a) Impedance magnitude and (b) phase spectra. The comparison includes the nominal model response (green dashed line), the experimental measurement (orange solid line), and the optimized model response (blue dashed line).

4.3. Parameter estimation of polymer samples

Following the calibration of the active element, the second stage involved coupling the PZT disc with the polymeric test samples (PLA, ABS, PET-G, PMMA, and Epoxy) using a thin acoustic coupling gel. In the numerical model, this interface was treated as a fluid layer with properties analogous to water (density of $1020\,\mathrm{kg\,m^{-3}}$ and speed of sound of $1480\,\mathrm{m\,s^{-1}}$). Based on the experimental measurements, a nominal thickness of $20\,\mu\mathrm{m}$ was adopted to identify the viscoelastic properties of the solid layers using the RP-UEIS method described in Section 3.5.

To assess the sensitivity of the impedance response to the coupling gel layer thickness, a forward numerical analysis was subsequently conducted on the calibrated PZT-PLA setup. In this step, the gel thickness was assumed to be 5, 20, and $50\,\mu\mathrm{m}$, while keeping the identified PLA parameters constant. Fig. 6 compares the PZT-PLA experimental impedance with the numerical reconstructions obtained for the coupled system under these three interface conditions. The visual observation is corroborated quantitatively by evaluating the MAPE of the impedance profiles. The baseline calibrated model with a $20\,\mu\mathrm{m}$ layer yielded a MAPE of 25.91%. When the thickness was reduced to $5\,\mu\mathrm{m}$ in the simulation, the error showed a negligible change (26.19%), indicating low sensitivity in the ultra-thin regime. In contrast, increasing the thickness to $50\,\mu\mathrm{m}$ resulted in a notable degradation of the fit, with the MAPE rising to 32.82%.

Table 4 summarizes the viscoelastic parameters identified using the RP-UEIS method within a ±12% bandwidth around the thickness mode resonance. The results clearly distinguish homogeneous cast polymers (PMMA and epoxy) from 3D-printed thermoplastics (PLA, ABS, PET-G). The PMMA sample exhibits the highest Young's modulus ($E' = 4.2691$ GPa) and longitudinal sound speed ($c_l = 2698.7$ m/s). When compared to the results of Ref. [20], the storage elastic parameters for this sample agree within 2%.

For epoxy, the Young's modulus ($E' = 2.5023\,\mathrm{GPa}$) is slightly lower than that of the PLA sample, which is the most elastic thermoplastic in this case. However, epoxy presents significantly higher longitudinal and shear losses, indicating it may act as an efficient acoustic absorber.

The identified sound speeds fall within typical high-frequency literature ranges. The homogeneous samples agree with bulk ultrasonic measurements [11] and full-parameter UEIS data [20], whereas the FDM samples are consistent with ultrasonic studies of 3D-printed polymers [13]. The reduced densities and higher attenuation observed in the thermoplastics are consistent with FDM-induced porosity, filament interfaces, and microstructural scattering. Overall, the elastic parameters are mechanically plausible, while the loss coefficients should be interpreted as effective values combining intrinsic viscoelastic damping and fabrication-induced scattering.

4.4. Applications to polymer-based acoustochips

The RP-UEIS method is next applied to the design of polymer-based acoustofluidic chips. The purpose of this example is not to reproduce the complete dissipative dynamics of the device, but rather to demonstrate that the material parameters identified through RP-UEIS constitute a physically consistent first approximation for acoustofluidic device design. The simplified acoustic model employed here neglects

Table 4
Estimated physical parameters of polymer materials via RP-UEIS method within 10% frequency bandwidth centered at 1.033 MHz.

Parameter	Symbol	PLA	ABS	PET-G	PMMA	Epoxy	Units
Density	ρ_s	1131.7	923.1	1199.6	1166.3	1018.9	$kg\,m^{-3}$
Young's modulus	E	2.57 − 0.13i	1.86 − 0.15i	2.22 − 0.48i	4.27 − 0.49i	2.50 − 0.60i	GPa
Poisson's ratio	ν	0.380 + 0.005i	0.379 + 0.008i	0.439 + 0.013i	0.390 + 0.013i	0.409 + 0.022i	–
Bulk modulus	K	3.57 − 0.03i	2.57 − 0.02i	6.00 − 0.00i	6.45 − 0.10i	4.56 − 0.00i	GPa
Shear modulus	G	0.93 − 0.05i	0.67 − 0.06i	0.77 − 0.17i	1.53 − 0.19i	0.88 − 0.23i	GPa
Long. sound speed	c_l	2062.2	1939.7	2420.6	2698.7	2373.9	$m\,s^{-1}$
Shear sound speed	c_s	907.5	854.6	800.4	1147.0	931.8	$m\,s^{-1}$
Long. tangent loss	$\tan\delta_l$	0.020	0.029	0.033	0.030	0.053	–
Shear tangent loss	$\tan\delta_s$	0.056	0.085	0.225	0.124	0.257	–
Long. absorption	α_l	271.6	420.2	387.4	318.4	631.2	$dB\,m^{-1}$
Shear absorption	α_s	1716.2	2790.1	7973.7	3109.0	7824.9	$dB\,m^{-1}$

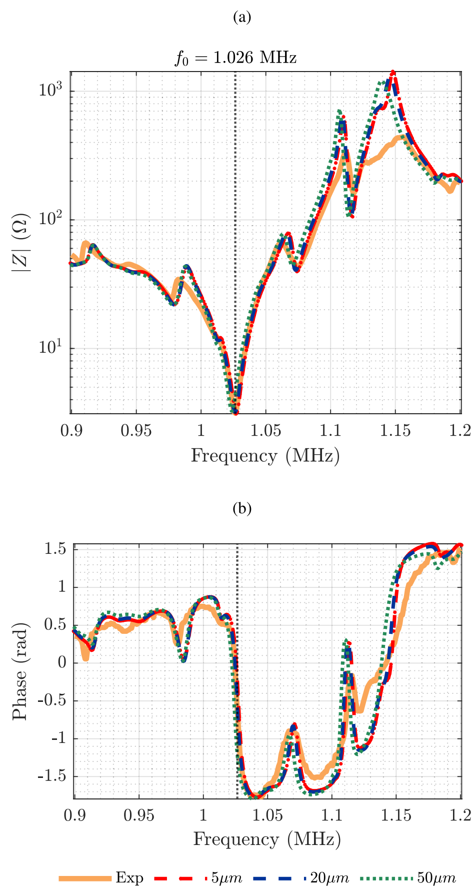

Fig. 6. Impedance fitting for the PZT+PLA configuration considering three coupling-gel thicknesses (5, 20, and 50 μm). (a) Impedance magnitude and (b) phase angle as a function of frequency. The numerical predictions for thinner layers align closely with the experimental spectrum. Vertical dotted line delimits the fundamental thickness-mode resonance.

thermoviscous losses in the cavity and viscous dissipation in the coupling gel layer. Consequently, quantitative prediction of the resonance linewidth and quality factor is outside the scope of the present model.

After experimentally identifying the mechanical properties of the constituent materials (PLA, epoxy, and PZT), these parameters are incorporated into finite-element simulations to guide the device design according to the desired acoustic response. In the present case, the objective is to generate a standing-wave field capable of levitating and aggregating microparticles at the pressure node located near the cavity center at mid-height.

Fig. 7 compares the impedance magnitude and phase of the acoustochip with an empty (air-filled) cavity and with the cavity filled

Table 5
Summary of the acoustochip performance parameters for empty and water-filled cavity states.

Metric	State	Exp	Num	Error (%)
f_0 (MHz)	Empty	1.0284	1.0286	0.02
	Filled	1.0274	1.0306	0.31
Z_{min} (Ω)	Empty	3.01	3.24	7.56
	Filled	4.10	4.04	1.46
Q factor	Empty	113.89	114.29	0.35
	Filled	85.33	103.06	20.77

with water. Table 5 summarizes the corresponding performance metrics, including the resonance frequency (f_0), the minimum impedance magnitude (Z_{min}), and the mechanical quality factor ($Q = f_0/\Delta f$, where Δf is the half-power bandwidth of the resonance). The Q factor corresponds to the electromechanical resonance of the entire multilayer chip structure, obtained from the electrical impedance spectrum.

The parameters f_0, Z_{min}, and Q factor show very good agreement between experiment and model, with frequency errors below 0.5%. The predicted impedance minima also match closely, indicating that the electromechanical coupling and effective stiffness of the multilayer stack are well captured by the numerical model.

The discrepancy observed in the Q factor for the water-filled cavity is consistent with the simplified acoustic model adopted here, which neglects thermoviscous boundary-layer losses and other fluid-related dissipation mechanisms. A more detailed thermoviscous formulation would likely improve the quantitative prediction of the resonance linewidth. However, the objective of the present study is the characterization of material parameters via RP-UEIS rather than the complete modeling of fluid dissipation.

Fig. 8 illustrates the simulated axial displacement field (u_z) in the solid components of the acoustochip, excited by a 10 V_{pp} sinusoidal signal. The fluid-filled cavity and thin coupling gel layer are masked in white, as they are modeled as fluid domains where structural displacement is not computed. The simulation shows a displacement antinode located at the center of the substrate–fluid interface (directly beneath the cavity), with a maximum amplitude of approximately 54 nm. This localized vibration acts as a piston-like source, efficiently transferring acoustic energy into the water layer and establishing the standing-wave field inside the cavity.

Fig. 9 presents the numerical Gor'kov potential (U) [28] associated with the acoustic radiation force acting on a probe polystyrene microparticle of diameter 10 μm for the designed acoustochip. Panel (a) illustrates the spatial distribution of U in the rz-plane, where a potential well (dark blue) appears at the cavity center with an approximately parabolic shape. Panel (b) shows the corresponding potential profiles along the lines $r = 0$ and $z = 3.25$ mm, the latter corresponding to the axial location of the potential minimum. The radial profile reveals the merging of two adjacent minima into nearly a single central potential well, which promotes the trapping of microparticles in this region. The corresponding acoustic radiation force is estimated to be of the order of

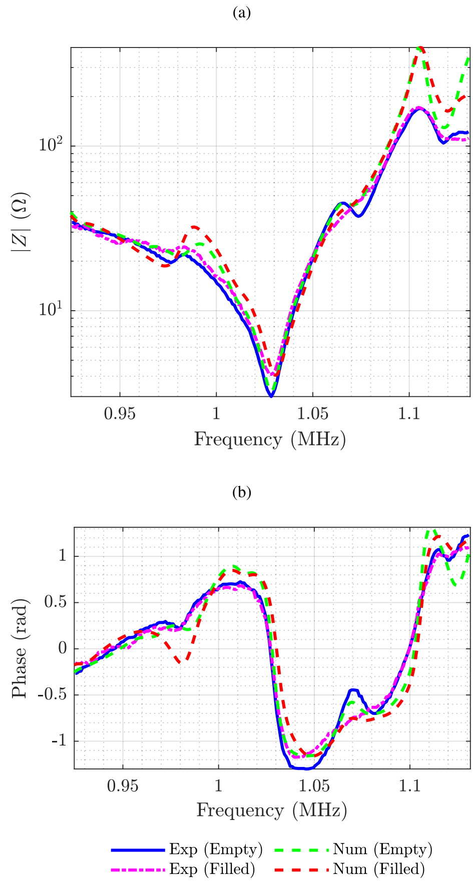

Fig. 7. Numerical and experimental data of the acoustofluidic chip of the impedance (a) magnitude and (b) phase for an "empty" (air-filled) and water-filled cavity.

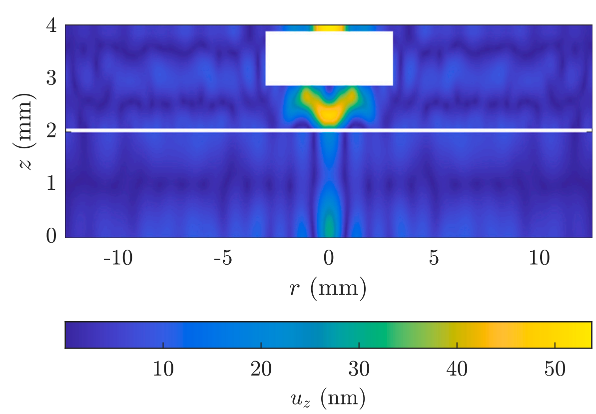

Fig. 8. Finite-element simulation results of the acoustochip. (a) Axial displacement field (u_z) at the resonance frequency (f_0 = 1.0274 MHz) with a 10 V_{pp} excitation. The white regions correspond to the fluid-filled cavity and thin coupling gel layer.

100 nN, which is several orders of magnitude larger than the opposing gravitational force acting on the particle. This force imbalance ensures stable acoustic trapping of microparticles near the cavity center.

Fig. 10 presents the experimental demonstration of microparticle trapping in the acoustochip. Panel (a) shows a photograph of the device, where a cluster of microparticles appears as a white cloud located near the center of the circular observation window. Panel (b) shows a micrograph confirming that the particles are tightly aggregated

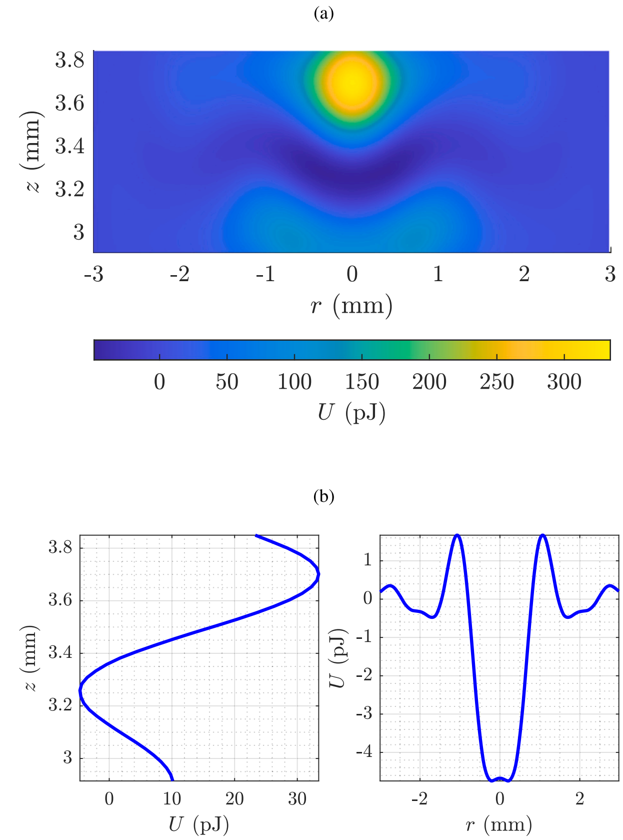

Fig. 9. Numerical results for the Gor'kov energy potential for a 10 µm polystyrene particle. (a) Potential spatial distribution at the rz plane. (b) Axial ($r = 0$) and radial $z = 3.25$ mm potential profiles.

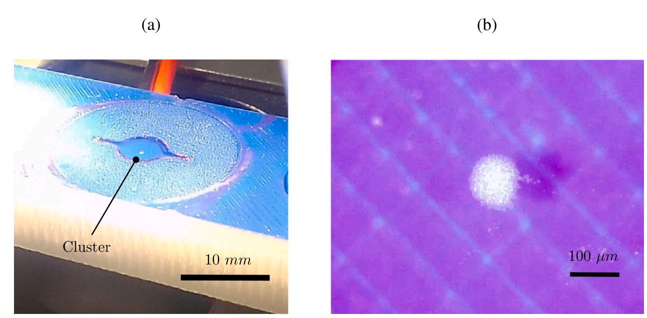

Fig. 10. Experimental validation of particle aggregation. (a) Photograph of the acoustochip positioned on the microscope stage; the arrow indicates the location of the stable acoustic trap. (b) Microscopic image showing a compact cluster of 10 µm polystyrene beads formed at the center of the cavity under ultrasound excitation at 1.03 MHz with an applied voltage of 10 V_{pp}.

at the geometric center of the chip. This experimental observation validates both the effectiveness of the device design and the accuracy of the material properties characterized through the RP-UEIS method.

5. Summary and conclusion

In this work, we developed a comprehensive methodology to estimate the complex electromechanical parameters of a PZT disc together with the viscoelastic parameters of polymeric materials. The approach combines a low-cost electrical impedance spectroscopy setup with an inverse FEA fitting procedure to characterize the coupled dynamics of PZT discs and passive polymer structural layers. The method builds upon the UEIS framework [20], while reducing the dimensionality of the associated inverse optimization problem from 16 to 10 parameters through a sensitivity-based parameter selection strategy. In the original method, once the PZT parameters are known, the determination of the viscoelastic parameters of a sample typically requires approximately 10 h of computational time. In contrast, the RP-UEIS approach reduces this time to about 1 h, significantly accelerating the material characterization process while maintaining accurate estimation of the relevant parameters.

For the reference PZT-4 element, the extracted elastic, piezoelectric, and dielectric components revealed that important properties, such as shear stiffness and longitudinal permittivity, required adjustments of up to $\sim$17.5 % and $\sim$14.6 % relative to manufacturer datasheets. Furthermore, the method successfully quantified the material's mechanical and dielectric dissipation, consistent with hard piezoceramic behavior at MHz frequencies. These discrepancies underscore the inadequacy of standard low-frequency data for megahertz regime predictions and confirm the reliability of the custom instrumentation to recover physically meaningful complex parameters.

The viscoelastic parameters obtained for the FDM thermoplastics (PLA, ABS, and PET-G) are broadly consistent with the values reported in the ultrasonic characterization study of Oliveira et al. [13] Although some differences in Young's and shear moduli are observed, particularly for PET-G, the estimated parameters remain within the same order of magnitude. These deviations are expected due to differences in printing conditions, internal porosity, and filament bonding inherent to FDM manufacturing. It should also be noted that the two characterization approaches operate at slightly different frequency regimes. In the present work, the parameters are extracted from impedance spectra near the transducer thickness-mode resonance around 1.03 MHz, whereas the ultrasonic transmission measurements reported by Oliveira et al. employ longitudinal and shear transducers operating at approximately 1 MHz and 2.25 MHz, respectively. For the homogeneous cast PMMA sample, the elastic parameters obtained here are also consistent with those reported by Bodé et al. [20] using the full UEIS framework, which was applied to polymer rings bonded to a PZT disc and analyzed over a broad impedance spectrum extending from hundreds of kilohertz to several megahertz. The agreement across these independent methodologies supports the physical plausibility of the parameters obtained with the RP-UEIS approach.

The RP-UEIS framework was further showcased as a practical tool for the design and predictive modeling of an acoustofluidic chip (made of PLA material) containing a circular half-wavelength resonator. By incorporating the experimentally identified viscoelastic parameters of the structural polymer layers into the finite-element model, the electromechanical response of the complete multilayer device could be simulated in a physically consistent manner. The obtained experimental results show that the calibrated model accurately reproduces the impedance spectra of the assembled acoustochip, including the resonance frequency and the minimum impedance magnitude, with deviations below 1% for the resonance frequency and below 10% for the impedance magnitude. Furthermore, the predicted acoustic field inside the cavity is consistent with the experimentally observed aggregation of microparticles at the pressure node, confirming the formation of a stable half-wavelength standing wave within the fluid chamber.

In summary, the RP-UEIS framework provides a practical methodology for identifying the complex viscoelastic parameters of polymer materials and incorporating them into predictive models of multilayer acoustofluidic devices. By combining a low-cost electrical impedance spectroscopy setup with a reduced-parameter inverse finite-element fitting procedure, the dimensionality and computational cost of the parameter identification problem are reduced. The proposed inverse methodology is not intrinsically limited to a single transducer element. In principle, it can be applied to array-based transducers. The RP-UEIS method offers a practical pathway for the characterization of polymer materials and the systematic design of polymer-based acoustofluidic devices.

CRediT authorship contribution statement

Jhoan F. Acevedo-Espinosa: Writing – original draft, Validation, Software, Methodology, Investigation, Conceptualization. **Flávio O.S. D'Amato:** Validation, Methodology, Investigation. **Marcos V.D. Vermelho:** Validation, Investigation. **Alana K.X.B. Branco:** Project administration, Methodology. **Antônio A.O. Carneiro:** Methodology, Investigation. **Michäel Baudoin:** Methodology, Investigation. **Joao L. Ealo:** Supervision, Conceptualization. **Glauber T. Silva:** Writing – review & editing, Supervision, Resources, Project administration, Formal analysis.

Declaration of AI-assisted technologies in the manuscript preparation process

During the preparation of this work the authors used ChatGPT (OpenAI, USA) in order to assist with language editing and improving the clarity of the manuscript. After using this tool/service, the authors reviewed and edited the content as needed and take full responsibility for the content of the published article.

Declaration of competing interest

The authors declare that they have no known competing financial interests or personal relationships that could have appeared to influence the work reported in this paper.

Acknowledgments

This study was supported by the National Council for Scientific and Technological Development–CNPq (Brazilian Agency), grant nos. 444099/2023-9, 173511/2023-6, and 302485/2023-6; and by the Coordination for the Improvement of Higher Education Funding Authority for Studies and Projects, Personnel–CAPES (Brazilian agency), grants nos. 88881.711904/2022-01 and 88881.010181/2024-00. More funding came from Funding Authority for Studies and Projects– FINEP (Brazilian agency), grant no. 1098/24-CETIS; iSOP Base project, supported by the Centro de Competência EMBRAPII VIRTUS em Hardware Inteligente para Indústria – VIRTUS-CC, with financial resources from the PPI HardwareBR of the MCTI (grant no. 055/2023), under agreement with EMBRAPII; and National Institute of Science and Technology in Innovative Research in Health Sciences–from Nanotechnology to Artificial Intelligence (CNPq-INCT PICS), grant no. 408417/2024-2.

Appendix. Power dissipation in piezoelectric materials

The instantaneous rate of mechanical and electrical work per unit volume performed on a piezoelectric material is given by

$$W(t) = \sigma_{ij}(t)\,\dot{\epsilon}_{ij}(t) + E_i(t)\,\dot{D}_i(t), \tag{A.1}$$

where the superposed dot denotes a time derivative. The first term represents the mechanical power associated with the stress–strain interaction, while the second term corresponds to the electrical power supplied to the material through the evolution of the electric displacement. The quantity $W(t)$ therefore measures the instantaneous power density converted into internal (recoverable) energy and irreversible heat (dissipated power).

Consider the time average identity for two complex amplitude functions $\overline{\mathrm{Re}[F\mathrm{e}^{-\mathrm{i}\omega t}]\,\mathrm{Re}[G\mathrm{e}^{-\mathrm{i}\omega t}]} = (1/2)\,\mathrm{Re}[FG^*]$. We also note that $\dot{\epsilon}_{ij} = -\mathrm{i}\omega\epsilon_{ij}$ and $\dot{D}_i = -\mathrm{i}\omega D_i$. We obtain for the power dissipation density

$$P_\mathrm{d} = \overline{W(t)} = \frac{\omega}{2}\,\mathrm{Im}\left[\sigma_{ij}\epsilon^*_{ij} + E_i D^*_i\right]. \tag{A.2}$$

For a passive transversely isotropic piezoelectric medium, we have $P_\mathrm{d} \geq 0$.

In the Voigt matrix notation, noting that $\sigma_{ij}\epsilon^*_{ij} = \epsilon^\dagger_{\mathrm{V}}\boldsymbol{\sigma}_{\mathrm{V}}$ and $E_i D^*_i = \boldsymbol{E}^\dagger \boldsymbol{D}$, we can write

$$P_{\mathrm{d}} = \frac{\omega}{2}\,\mathrm{Im}\left[\epsilon^\dagger_{\mathrm{V}}\boldsymbol{\sigma}_{\mathrm{V}} + \boldsymbol{E}^\dagger\boldsymbol{D}\right] = \frac{\omega}{2}\,\mathrm{Im}\left(\begin{bmatrix}\epsilon_{\mathrm{V}}\\ \boldsymbol{E}\end{bmatrix}^\dagger \begin{bmatrix}\boldsymbol{\sigma}_{\mathrm{V}}\\ \boldsymbol{D}\end{bmatrix}\right). \tag{A.3}$$

Using Eq. (12), we can write

$$P_{\mathrm{d}} = \frac{\omega}{2}\,\mathrm{Im}\left[\left(\mathbf{M}\begin{bmatrix}\epsilon_{\mathrm{V}}\\ \boldsymbol{E}\end{bmatrix}\right)^\dagger \begin{bmatrix}-\epsilon_{\mathrm{V}}\\ \boldsymbol{E}\end{bmatrix}\right] = \frac{\omega}{2}\,\mathrm{Im}\left(\begin{bmatrix}\epsilon_{\mathrm{V}}\\ \boldsymbol{E}\end{bmatrix}^\dagger \mathbf{M} \begin{bmatrix}-\epsilon_{\mathrm{V}}\\ \boldsymbol{E}\end{bmatrix}\right)$$
$$= \frac{\omega}{2}\,\mathrm{Im}\left(\begin{bmatrix}\epsilon_{\mathrm{V}}\\ \boldsymbol{E}\end{bmatrix}^\dagger \mathbf{K} \begin{bmatrix}\epsilon_{\mathrm{V}}\\ \boldsymbol{E}\end{bmatrix}\right) \geq 0, \quad \mathbf{K} = \begin{bmatrix}-\boldsymbol{C}_{\mathrm{V}} & \mathbf{e}^T\\ \mathbf{e} & \boldsymbol{\varepsilon}\end{bmatrix}. \tag{A.4}$$

This implies that Im[$\mathbf{K}$] must be positive definite. In practical terms, this implies that all of its eigenvalues must be non-negative, which readily imposes the constraints

$$C''_{12} \geq C''_{11}, \quad C''_{44} \leq 0, \quad C''_{66} \leq 0, \quad \varepsilon''_{11} \geq 0, \quad \varepsilon''_{33} \geq 0, \tag{A.5a}$$

$$C''_{11} + C''_{12} + C''_{33} \leq -\sqrt{R}, \tag{A.5b}$$

where

$$R = C''^{\,2}_{11} + 2C''_{11}C''_{12} - 2C''_{11}C''_{33} + C''^{\,2}_{12} - 2C''_{12}C''_{33} + 8C''^{\,2}_{13} + C''^{\,2}_{33}. \tag{A.6}$$

Data availability

Data will be made available on request.

References

[1] T.L. Szabo, Diagnostic Ultrasound Imaging: Inside Out, Elsevier Acad. Press, 2004.

[2] P. Reynolds, S.M. Spearing, Surface acoustic wave sensors, Proc. IEEE 99 (2) (2011) 258–271, http://dx.doi.org/10.1109/JPROC.2010.2089637.

[3] E. Cesewski, A.P. Haring, Y. Tong, M. Singh, R. Thakur, S. Laheri, K.A. Read, M.D. Powell, K.J. Oestreich, B.N. Johnson, Additive manufacturing of three-dimensional (3d) microfluidic-based microelectromechanical systems (mems) for acoustofluidic applications, Lab Chip 18 (2018) 2087–2098.

[4] F. Lickert, M. Ohlin, H. Bruus, P. Ohlsson, Acoustophoresis in polymer-based microfluidic devices: Modeling and experimental validation, J. Acoust. Soc. Am. 149 (2021) 4281–4291.

[5] N. Jeger-Madiot, L. Arakelia, N. Setterblad, P. Bruneval, M. Hoyos, J. Larghero, J.-L. Aider, Self-organization and culture of mesenchymal stem cell spheroids in acoustic levitation, Sci. Rep. 11 (2021) 8355.

[6] H.D.A. Santos, A.E. Silva, G.C. Silva, E.B. Lima, A.S. Marques, M.S. Alexandre-Moreira, A.C. Queiroz, C. Jacinto, J.H. Lopes, U. Rocha, G.T. Silva, 3D-printed acoustofluidic devices for Raman spectroscopy of cells, Adv. Eng. Mater. 23 (2021) 2100552.

[7] U. Rocha, G.C. Silva, M.V.S. Sales, F.O.S. D'Amato, A.C.R. Leite, G.T. Silva, Advancing Raman spectroscopy of erythrocytes with 3D-printed acoustofluidic devices, Appl. Phys. Lett. 123 (2023) 034105.

[8] K.S.C. Borbely, F.O.S. D'Amato, K.S.Q. da Silva, D.W.S. França, A.L.M. Silva, A.F.S. Lima, A.U. Borbely, G.T. Silva, Toward cell microculture using acoustofluidics technology, in: A.B. Soares, R.F. Leoni, G.C. Cardoso (Eds.), XXIX Brazilian Congress on Biomedical Engineering, in: IFMBE Proc., Vol. 126, Springer, Cham, 2025, pp. 28–32, http://dx.doi.org/10.1007/978-3-031-94921-0_4.

[9] A. Migliori, J.L. Sarrao, Resonant ultrasound spectroscopy: Applications to physics, materials measurements, And Nondestructive Evaluation, Wiley, 1997.

[10] I.I. Popov, M.V. Shitikova, Impulse excitation technique and its application for identification of material damping: an overview, IOP Conf. Ser. : Mater. Sci. Eng. 962 (2020) 022025.

[11] M. Sinha, D.J. Buckley, Acoustic properties of polymers, in: Physical Properties of Polymers Handbook, Springer, 2007, pp. 1021–1031.

[12] F. Lionetto, A. Maffezzoli, Polymer characterization by ultrasonic wave propagation, Adv. Polym. Technol. 27 (2008) 63–73.

[13] T.F. de Oliveira, A.C. Cavalheiro, F. Buiochi, M.S. Tsuzuki, J.P. Leão-Neto, G.C. Silva, G.T. Silva, J.H. Lopes, Ultrasonic characterization of 3d-printed polymer objects, Ultrasonics 149 (2025) 107572.

[14] J.G. Smits, Piezoelectric transducers and resonators: An equivalent circuit approach, IEEE Trans. Sonics Ultrason. 23 (1976) 393–402, http://dx.doi.org/10.1109/T-SU.1976.30964.

[15] S. Sherrit, H.D. Wiederick, B.K. Mukherjee, S.A. Butler, Characterization of piezoelectric materials for transducers using electrical impedance measurements, IEEE Trans. Ultrason. Ferroelectr. Freq. Control 46 (1999) 1140–1150.

[16] N. Bretz, J. Strobel, M. Kaltenbacher, R. Lerch, Inverse determination of material parameters for piezoelectric resonators, in: Proc. IEEE Int. Ultrason. Symp., 2005, pp. 703–706, http://dx.doi.org/10.1109/ULTSYM.2005.1602970.

[17] W.P. Mason, Electromechanical transducers and wave filters, J. Acoust. Soc. Am. 20 (1948) 523–534, http://dx.doi.org/10.1121/1.1906406.

[18] R. Krimholtz, D.A. Leedom, G.L. Matthaei, New equivalent circuits for elementary piezoelectric transducers, Electron. Lett. 6 (1970) 398–399, http://dx.doi.org/10.1049/el:19700280.

[19] W.S. Na, J. Baek, A review of the piezoelectric electromechanical impedance based structural health monitoring technique for engineering structures, Sensors 18 (5) (2018) 1307.

[20] F. Lickert W.N. Bodé, P. Augustsson, H. Bruus, Determination of the complex-valued elastic moduli of polymers by electrical-impedance spectroscopy for ultrasound applications, Phys. Rev. Appl. 18 (2022) 064078, http://dx.doi.org/10.1103/PhysRevApplied.18.064078.

[21] R. Lerch, Simulation of piezoelectric devices by two- and three-dimensional finite elements, IEEE Trans. Ultrason. Ferroelectr. Freq. Control 37 (1990) 233–247, http://dx.doi.org/10.1109/58.56195.

[22] A. Tarantola, Inverse Problem Theory and Methods for Model Parameter Estimation, SIAM, Philadelphia, PA, USA, 2005.

[23] Ieee standard on piezoelectricity, Tech. Rep. ANSI/IEEE Std, IEEE, New York, NY, USA, 1988, pp. 176–1987.

[24] F. Li, Z. Xu, X. Wei, X. Yao, Determination of temperature dependence of piezoelectric coefficients matrix of lead zirconate titanate ceramics by quasi-static and resonance method, J. Phys. D: Appl. Phys. 42 (2009) 095417, http://dx.doi.org/10.1088/0022-3727/42/9/095417.

[25] A. Saltelli, Sensitivity analysis for importance assessment, Risk Anal. 22 (2002) 579–590, http://dx.doi.org/10.1111/0272-4332.00040.

[26] L. Tang, W. Cao, Temperature dependence of self-consistent full matrix material constants of lead zirconate titanate ceramics, Appl. Phys. Lett. 106 (2015) 052902.

[27] B. Kar, H. Basaeri, S. Roundy, U. Wallrabe, Complex piezoelectric material parameters of hard pzt determined from a single disc transducer, Smart Mater. Struct. 32 (8) (2023) 085012.

[28] L.P. Gor'kov, On the forces acting on a small particle in an acoustic field in an ideal fluid, Sov. Phys. Dokl. 6 (9) (1962) 773–775.